On the design of mesostructured acidic catalysts for the one-pot dimethyl ether production from CO_2

Claudio Cara,[1,2§] Fausto Secci, [1§] Sarah Lai,[3] Valentina Mameli,[1,2] Kai Skrodczky,[4] Patricia A. Russo,[4] Francesca Ferrara[3], Elisabetta Rombi,[1] Nicola Pinna,[4] Mauro Mureddu,[3*] Carla Cannas[1,2*]

[1]*Department of Chemical and Geological Sciences, University of Cagliari, S.S. 554 bivio per Sestu, 09042 Monserrato (CA), Italy*

[2]*Consorzio Interuniversitario Nazionale per la Scienza e Tecnologia dei Materiali (INSTM), Via Giuseppe Giusti 9, 50121 Firenze (FI), Italy*

[3]*Sotacarbo S.p.A., Grande Miniera di Serbariu, 09013, Carbonia (SU), Italy*

[4]*Institut für Chemie and IRIS Adlershof, Humboldt-Universität zu Berlin, 12489 Berlin, Germany*

**Corresponding authors*

[§]Equal contribution

Abstract

Dimethyl ether (DME) production from hydrogenation of CO_2 based on two-function (redox and acidic) catalysts is receiving increasing attention due to the high demand for alternative and green fuels. In this work, we propose different mesostructured acidic metal oxides as methanol dehydration catalysts to be used as physical mixtures in combination with a commercial Cu-based redox catalyst (CZA) for the CO_2-to-DME one-pot production. Al-MCM-41, TiO_2 and TiO_2-ZrO_2 mixed oxides, obtained through Sol-Gel methods, either in a conventional or Evaporation-Induced Self-Assembly approach were selected as mesostructured acidic systems and compared with a commercial zeolite (ferrierite). The regular mesoporous structure should render the active sites of the acidic catalyst easily accessible for CO_2 and H_2 and allow a homogeneous dispersion of the redox phase inside the mesopores in view of a possible development of bifunctional catalysts (redox + acidic). With the aim of understanding how the textural and acidic properties can be correlated with the performances and eventually design efficient dehydration catalysts, a careful study on the acidic sites was performed by both adsorption microcalorimetry with ammonia and FTIR-monitored adsorption of pyridine. The results of the performances highlighted a higher activity toward methanol dehydration for catalysts featured by Brønsted sites (zeolite and Al-MCM-41); as for catalysts with Lewis sites only (TiO_2, $Ti_{0.77}Zr_{0.23}O_2$) better performances were shown in case of

systems presenting sites of moderate strength ($Ti_{0.77}Zr_{0.23}O_2$). In the light of the above, Al-MCM-41 and TiO_2-ZrO_2 demonstrated to be the most promising mesostructured dehydration catalysts in terms of selectivity to DME.

Keywords: mesostructured materials • dimethyl ether • CO_2 conversion • catalysis • methanol dehydration

1. Introduction

In the last two decades, dimethyl ether (DME) has received more and more attention due to its potential in substituting diesel as fuel [1–10]. Its industrial production is based on a two-step process in which methanol is first produced from syngas using a Cu-based catalyst and subsequently dehydrated over an acidic catalyst to obtain DME [10,11]. γ-Al_2O_3 is the traditional industrial acidic catalyst for methanol dehydration thanks to its high DME selectivity, but it suffers from suppression of its catalytic activity, due to the competitive adsorption of water on its acidic sites [12]. Starting from the progress made in syngas-to-DME conversion, CO_2-to-DME production is taking place in the last decade, due to the possibility of revaluating CO_2, no longer as a waste, but as a valuable reagent. This strategy aims to contribute to solve several critical challenges; the increasing demand of renewable fuels together with the need to substitute the fossil sources with raw materials featuring a low or zero-carbon footprint, encouraging the research of alternative pathways for the production of DME. For this reason, there is a growing interest around DME production technologies based on CO_2 hydrogenation, where the feedstocks are either captured or biogenic CO_2 and green H_2 (e.g. produced from non-fossil pathways such as electrolysis fed by renewable sources). In this context, DME can be obtained from CO_2 through these two subsequent reactions [5,13]:

$$CO_2 + 3H_2 \leftrightarrows CH_3OH + H_2O \qquad \Delta H^0_{298K} = -49.5 \text{ kJ/mol} \qquad \text{Redox reaction} \qquad (1)$$

$$2CH_3OH \leftrightarrows CH_3OCH_3 + H_2O \qquad \Delta H^0_{298K} = -23.4 \text{ kJ/mol} \qquad \text{Dehydration reaction} \qquad (2)$$

Nevertheless, DME can also be produced in a one-step process that should be more efficient than the two-step route, mainly because methanol dehydration to DME promotes the CO_2 conversion [14]. As reported for the production of DME from syngas, the most widely investigated systems for CO_2 conversion to methanol are Cu-based catalysts; the most promising ones are based on ternary systems (CuO/ZnO/γ-Al_2O_3; CuO/ZnO/ZrO_2) in which copper is the active phase, ZnO acts as a promoter, and the third phase usually increases the thermal and chemical stability of the catalyst [5,12,15]. As of dehydration catalysts, the most promising ones are zeolites, mainly ZSM-5 (MFI) and ferrierite (FER) in their acidic form (H-zeolite), due to their high dehydration performances deriving

from their acidic sites in a microporous crystalline framework. γ-Al_2O_3 has also been reported due to its high selectivity to DME but, like in the case of the DME production from syngas, it suffers from deactivation due to adsorption of water, deriving from the dehydration of methanol, on its Lewis acidic sites, the only acidic species present on γ-Al_2O_3 [12,16]. Furthermore, in the CO_2 to DME reaction, water is also produced in the first step of the reaction (CO_2 hydrogenation), unlike in the case of syngas, which does not give rise to water production. Consequently, γ-Al_2O_3 deactivation is much more prominent in CO_2 to DME reaction. Unlike γ-Al_2O_3, zeolites have shown a much higher tolerance to deactivation due to water adsorption [17,18]; this phenomenon can be explained by the presence of Brønsted acidic sites. Furthermore, Brønsted sites have demonstrated to be much more active in terms of methanol conversion to DME in both two-step and one-step processes [18]; however, the presence of strong Brønsted acidic sites can lead to the formation of undesired by-products, mainly olefins and coke [12]. In rare cases, TiO_2 [19], ZrO_2 [19] and mixed oxides [19] have also been reported, as like as some mesostructured aluminosilicates (Al-MCM-41, Al-SBA-15) [20–23]. TiO_2, ZrO_2, and Ti-Zr mixed oxides have shown only Lewis acidic sites, weaker than those of γ-Al_2O_3 [19] and thus less prone to deactivation due to water adsorption, leading to a high selectivity to DME, whereas the mesostructured aluminosilicates have shown both Lewis and Brønsted acidity [24–26]. Acidic and redox catalysts are usually combined as physical mixtures through solid phase or liquid phase mixing [12,15]. In solid phase mixing, the two catalysts are simply mixed together in powder phase; in liquid phase mixing, they are dispersed into a proper solvent and finally recovered by solvent evaporation. In some other cases the two different catalysts are not mixed together but rather laid into the reactor in two subsequent layers [5]. Recently, in the literature, some authors have proposed composite catalysts for the one-pot production of DME [12,15]. In most cases, these catalysts, named hybrid by some authors [12,15], and here reported as bifunctional catalysts, consist of a solid support (usually the dehydrating phase) on which the redox phase is dispersed by a chemical route [12]. These composite catalysts are commonly obtained on porous acidic solids, mainly zeolites [27–30], in order to increase the area of contact between the two catalytic functions. A few cases of mesoporous/mesostructured solids functionalized with a redox phase have also been reported [31,32]; it should be emphasized that they mainly consist in mesostructured γ-Al_2O_3 impregnated with a Cu-based phase [33,34]. In this perspective, the use of mesoporous materials showing an ordered pore structure (mesostructure) as dehydrating supports, instead of zeolites, can be considered a valuable choice in view of designing bifunctional catalysts. In fact, the ideal pore size and the high surface area and pore volume should allow a maximization of the contact area

between the redox and the dehydration catalysts, granting a homogeneous dispersion of the redox phase inside the mesopores [31]. Furthermore, the presence of the pore walls should limit the growth of the redox phase particles, leading to the formation of a redox phase in form of confined nanoparticles [35], and prevent sintering phenomena, making the material stable and regenerable [36–40]. The presence of a framework with larger pores, compared to zeolites, should also improve the accessibility of the active sites of the catalyst during the reaction. Zeolites, on the contrary, do not present an ideal porous framework to act as supports for the development of bifunctional nanocomposite catalysts; the redox phase, indeed, cannot be dispersed inside the microporous structure of zeolites, due to the small pore diameter. Therefore, the redox phase can only be deposited on the external surface of zeolites, partially blocking the accessibility of the micropores to the molecules of reactants, and not allowing a fine tuning of the size and the dispersion of the redox phase. As a consequence, sintering phenomena cannot be inhibited, making these systems not regenerable. With that in mind, in this work, mesostructured dehydrants as an aluminosilicate (Al-MCM-41), pure titania (TiO_2) and a mixed oxide ($Ti_{0.77}Zr_{0.23}O_2$), rarely proposed in the literature, were developed and used in form of physical mixtures with a CuO/ZnO-based commercial redox catalyst (CZA). Their performances were compared with those of ferrierite, a commercial zeolite commonly proposed as dehydration catalyst, due to its better catalytic performances with respect to other commercial zeolites [14,41]. The type and strength of acidic sites were characterized and their effect on the performances of the catalysts were investigated. New insights were gathered, allowing a potential development of new acidic mesostructured catalysts by tailoring their acidic properties in order to maximize their performances for methanol dehydration.

2. Experimental section

2.1 Chemicals

All chemicals were used as received without further purification. Hexadecyltrimethylammonium bromide (CTAB, 98%), poly(ethylene glycol)-block-poly(propylene glycol)-block-poly(ethylene glycol) (PEG-PPG-PEG, Average M_W=5800 g·mol^{-1}, Pluronic® P-123), ethanol (EtOH, azeotropic 95.6% and EtOH, absolute >99.8%), titanium (IV) isopropoxide $Ti(OPr)_4$, 97%, tetraethyl orthosilicate (TEOS, 98%), ammonia solution (28-30% wt% of NH_3 in H_2O), hydrochloric acid (HCl, 36.5-38.0% wt%), sulfuric acid (H_2SO_4, 95.0-98.0 wt%) were purchased from Sigma-Aldrich. Aluminum isopropoxide $Al[OCH(CH_3)_2]_3$, 98%+, zirconium (IV) tert-butoxide $Zr(OBu)_4$, 97%+, copper-based methanol

synthesis catalyst (CZA), and zeolite ferrierite with molar ratio SiO_2:Al_2O_3 20:1 were supplied by Alpha Aesar.

2.2 Synthesis of Al-MCM-41

Aluminum-doped MCM-41 (Al-MCM-41) was synthesized by adapting a sol-gel method proposed by Cara *et al.* for MCM-41 [37]. Typically, 0.2314 g of aluminum isopropoxide were dissolved in 3.79 mL of TEOS into a vial. Separately, 1 g of the templating agent CTAB was dissolved in 200 g of bi-distilled water into a flask; the solution was kept under stirring at 30 °C, 300 RPM for 3.5 h. 69.1 g of absolute ethanol were then added and the solution was kept under stirring for other 20 minutes, 21 mL of NH_3 were then added and the stirring was increased to 600 RPM; the mixture of precursors previously prepared was then immediately added into the flask and the vigorous stirring at 600 RPM was kept for 5 minutes, until a milky white mixture was obtained. The stirring was then decreased back to 300 RPM and the reaction was carried out for 19 h at 30 °C; the obtained material was subsequently washed with a 1/1 water/ethanol solution and separated by centrifugation at 4500 RPM for three times, dried and eventually calcined at 550 °C to induce the decomposition of the templating agent.

2.3 Synthesis of mesostructured TiO_2/ZrO_2-based catalysts

Inspired by the sulfuric acid carbonization approach proposed by Zhao *et al.* for TiO_2 [42], the synthetic process was adapted to obtain mixed titania-zirconia oxides having a molar ratio of Ti=77% and Zr=23% in the case of the sample $Ti_{0.77}Zr_{0.23}O_2$, Ti=23% and Zr=77% for the sample $Ti_{0.23}Zr_{0.77}O_2$ and Ti=50% and Zr=50% for the sample $Ti_{0.50}Zr_{0.50}O_2$. Generally, 1 g of Pluronic® P123 was dissolved in 30 g of absolute ethanol (EtOH abs), 1.4 g of HCl 37 wt% and 0.46 g of H_2SO_4 44 wt% were added under vigorous magnetic stirring and the mixture was heated at 40 °C for 3 h under a nitrogen atmosphere. Then, a certain amount of $Ti(OPr)_4$ and $Zr(OBr_4)$ (**Table S1**) was added dropwise and left for further 20 h at the same temperature. The corresponding sol was poured into a Petri dish and evaporated for two days at 40 °C in air under 50-60% of relative humidity; the resultant film was aged at 100 °C for further two days. The obtained product was firstly treated at 450 °C (heating rate 1°C min^{-1}) under nitrogen atmosphere for 2 h, and subsequently calcined at 380 °C (heating rate 2 °C min^{-1}) under air for 2 h. It is worth mentioning that the samples showed a black shining color after the nitrogen thermal treatment, suggesting the formation of the amorphous carbon scaffold. Conversely, after calcination, they appeared as a light-yellow powder.

2.4 Characterization methods

Small-angle (SA-XRD, 2θ = 0.8°–7°) and wide-angle (WA-XRD, 2θ = 8°- 80°) X-ray diffraction patterns were recorded on a Seifert X3000 instrument with a θ−θ geometry featuring a Cu anode. The lattice parameter was calculated using the equation $a_0 = \frac{2d_{100}}{\sqrt{3}}$, assuming hexagonal pore structure for the mesostructured samples. The mean crystallite size of TiO_2, $<D_{XRD}>$, was obtained by Scherrer equation, assuming K equal to 0.9. $<D_{XRD}>$ was calculated as a mean value by fitting, through Origin software, the most intense X-ray peaks with the PseudoVoigt function, by using a 1:1 Gaussian: Lorentzian ratio (mu = 0.5).

Textural analyses were performed on a Micromeritics ASAP 2020 system by determining the nitrogen adsorption–desorption isotherms at -196 °C. Prior to the analyses, ferrierite and Al-MCM-41 samples were heated for 12 h under vacuum at 250 °C (heating rate, 1 °C min^{-1}), while the TiO_2/ZrO_2 samples were heated at 120 °C. The Brunauer–Emmett–Teller (BET) specific surface area was calculated from the adsorption data in the P/P_0 range 0.05-0.17 for Al-MCM-41 and 0.05-0.3 for the TiO_2/ZrO_2 samples. Due to the microporous nature of ferrierite, the specific surface area was estimate by using the Dubinin-Radushkevich model and the total pore volume and pore dimensions by the Horvath-Kawazoe model. For Al-MCM-41, TiO_2 and $Ti_{0.77}Zr_{0.23}O_2$ the total pore volume (V_p) was calculated at P/P_0 = 0.875, while mean pore diameter was determined by applying the Barrett−Joyner−Halenda (BJH) model to the desorption branch isotherm.

Transmission electron microscopy (TEM) images were obtained on a JEOL JEM 1400-PLUS microscope operating at an accelerating voltage of 120 kV. High-resolution TEM (HRTEM) images were carried out using a JEOL JEM 2010 UHR microscope equipped with a 794 slow-scan CCD camera operating at 200 kV. Finely ground powders of the samples were first dispersed in ethanol and sonicated. The resulting suspensions were dropped onto 200 mesh carbon-coated copper grids.

To perform adsorption–desorption in situ measurements, pyridine vapor was adsorbed at room temperature using specially designed quartz cells equipped with KBr windows and permanently connected to a vacuum line. The samples, in the form of self-supported pellets (10-20 mg in weight of sample), were preliminary outgassed at 250 °C under vacuum conditions (residual pressure $<1.3x10^{-5}$ Pa) for 6 h (heating rate 4 °C min^{-1}) and then cooled to room temperature prior to the pyridine adsorption experiments. A spectrum of the sample was acquired and used as blank for subtraction from the subsequent spectra, acquired after pyridine adsorption. The sample was

saturated with a proper amount of pyridine, then the FTIR spectrum was recorded (namely Saturated) with a Nicolet iS50 spectrometer (Thermo Fisher), then the line was evacuated and after 1 h a FTIR spectrum labelled Desorbed was recorded.

A Tian-Calvet heat flow calorimeter (Setaram) equipped with a volumetric vacuum line was used for the microcalorimetric measurements. Samples (about 100 mg) were pretreated overnight at 300 °C under vacuum (1 Pa) prior to the successive introduction of small doses of the probe gas (ammonia). The equilibrium pressure relative to each adsorbed amount was measured by means of a differential pressure gauge (Datametrics) and the thermal effect recorded. The run was stopped at a final equilibrium pressure of 133 Pa. The adsorption temperature was maintained at 80 °C, in order to limit physisorption. After overnight outgassing at this same temperature, a second run was carried out up to 133 Pa. The adsorption and calorimetric isotherms were obtained from each adsorption run. The adsorption isotherms relate the amount of probe gas with the corresponding equilibrium pressure. The overall uptake of the probe gas on the solid was assessed from the first isotherm ($n_{A,tot}$); the amount of the probe gas irreversibly adsorbed ($n_{A,irr}$) was calculated by subtracting from the first isotherm the second one, obtained after outgassing the sample. The calorimetric isotherms relate the integral heat of adsorption with the corresponding equilibrium pressure. Combining the adsorption and calorimetric data, a plot of the differential heat of adsorption as a function of the adsorbed amount was drawn, which gives information on the influence of the surface coverage on the energetics of the adsorption.

2.5 Catalytic tests

The DME synthesis experiments were carried out in a customized Microactivity Effi (PID Eng&Tech) bench-scale plant, employing a high-pressure fixed-bed stainless steel reactor (length 304.8 mm, inner diameter 9.1 mm). A porous plate (made of Hastelloy C, 20 µm) and quartz wool were used to support the catalytic bed inside the isothermal temperature zone of the reactor [41]. Tests were performed using physical mixtures made up of a commercial Cu-based redox catalyst (CZA) and the dehydration catalyst. The amount of physical mixture used for each run was fixed at 1 g of redox phase (CZA) and 1 g of acidic catalyst. When only the redox phase was tested, 1 g of CZA was used. The obtained catalytic systems have been diluted with a certain amount (1.5 g for the tests on physical mixtures, 2.5 g for the test on CZA only) of α-Al_2O_3, a chemically inert material, in order to reach a total bed volume of *ca.* 3 cm^3. As a result, keeping constant the inlet flow rate, the gas hourly

space velocity (GHSV) resulted to be 6000 $Ncm^3\ g_{cat}^{-1}\ h^{-1}$ for physical mixtures and 12000 $Ncm^3\ g_{cat}^{-1}\ h^{-1}$ for the test of the redox catalyst only.

Before the catalytic tests, all fresh catalysts were reduced in-situ in a stream of a H_2/N_2 mixture (H_2, 15 vol% in N_2) at 250 °C for 2 h under atmospheric pressure. Upon completion of the reduction process, the system was maintained at 250 °C, and the reaction gas mixture containing H_2 and CO_2 (molar ratio of 3:1) and 10 vol% of N_2 (used as internal standard for gas chromatographic analysis) was fed and the pressure was allowed to reach 3.0 MPa. After allowing the system to reach the steady state in 1 h on stream, analysis was periodically performed within the run; runs were carried out for at least 36 h. The reaction stream was analyzed by a 7890B (Agilent) gas chromatograph equipped with a flame ionized detector (FID) for carbon-containing compounds and with a thermal conductivity detector (TCD) for permanent gases. Two columns connected in series were used to identify the components of the outlet gas mixture. In particular, CO_2, methanol, dimethyl ether, ethane, and propane were separated by a HP-PLOT Q (Agilent) column (length 30 m, inner diameter 0.53 mm, film thickness 40 µm), while a HP-PLOT Molesieve (Agilent) column (length 30 m, inner diameter 0.53 mm, film thickness 50 µm) was used for H_2, N_2, CH_4, and CO. To avoid condensation of condensable products, the connection lines between the plant gas outlet and gas chromatograph inlet were heated at 180 °C. CO_2 conversion (X_{CO2}), products selectivity (S_P, with P: CH_3OH, DME, or CO), and products yield (Y_P, with P: CH_3OH or DME), were calculated as follows:

$$X_{\mathrm{CO_2}} = \frac{n_{\mathrm{CO_2}}^{\mathrm{in}} - n_{\mathrm{CO_2}}^{\mathrm{out}}}{n_{\mathrm{CO_2}}^{\mathrm{in}}} \times 100$$

$$S_{\mathrm{P}} = \frac{\nu_{\mathrm{CO_2}}}{\nu_{\mathrm{P}}} \times \frac{n_{\mathrm{P}}^{\mathrm{out}}}{n_{\mathrm{CO_2}}^{\mathrm{in}} - n_{\mathrm{CO_2}}^{\mathrm{out}}} \times 100$$

$$Y_{\mathrm{P}} = \frac{\nu_{\mathrm{CO_2}}}{\nu_{\mathrm{P}}} \times \frac{n_{\mathrm{P}}^{\mathrm{out}}}{n_{\mathrm{CO_2}}^{\mathrm{in}}} \times 100$$

where n_i^{in} and n_i^{out} are the number of moles of the *i*-th species in the feed or in the gas mixture exiting from the reactor, respectively, and v_i is the stoichiometric coefficient of the *i*-th species in the corresponding balanced equation.

In order to assess the error associated with the catalytic tests, a catalytic run using commercial catalysts was performed three times obtaining a standard deviation in the 2-5% range for both conversion and selectivity.

3. Results and discussion

3.1 Characterization of pristine samples

Figure 1a and **Figure 2a** depict wide-angle X-ray diffraction (WA-XRD) patterns of the samples ferrierite, Al-MCM-41, TiO_2, and $Ti_{0.77}Zr_{0.23}O_2$, the most promising binary Ti-Zr oxide in terms of degree of mesoporous order (see **Figure 2g, Figure 2h, S1e-h**). Other binary oxides, as $Ti_{0.23}Zr_{0.77}O_2$ and $Ti_{0.50}Zr_{0.50}O_2$, were synthesized (**Table S1**) and the results were reported in the supporting information (**Figure S1, Table S2)**; however, since TEM images (**Figure S1**) showed a lower degree of mesoporous order, the attention was focused only on $Ti_{0.77}Zr_{0.23}O_2$. The position and sharpness of the X-ray diffraction peaks (**Figure 1a**) of the ferrierite sample confirmed its microcrystalline nature (PDF card N. 00-039-1382). On the contrary, the sample Al-MCM-41 showed an amorphous nature as evinced by the presence of a broad band centered at about 23° (2θ). The XRD data proved that TiO_2 sample is constituted by nanocrystals of about 4 nm of anatase phase, (PDF card N. 00-021-1272) while $Ti_{0.77}Zr_{0.23}O_2$ is amorphous, as confirmed by the two broad bands (**Figure 2a**). Except for ferrierite, small angle X-ray diffraction patterns (SA-XRD, **Figure 1b** and **Figure 2b**) showed the presence of a well-defined ordered mesoporous structure. Nitrogen physisorption analysis further confirmed the mesoporous nature of the three samples, as well as the microporous nature of ferrierite (**Figures 1c, 1d, 2c, 2d**). **Table 1** reports the textural properties of the samples: Al-MCM-41 shows the highest surface area (1246 m^2g^{-1}), three times higher than that of ferrierite (415 m^2g^{-1}). TiO_2 and $Ti_{0.77}Zr_{0.23}O_2$ show surface areas of 273 and 183 m^2g^{-1}, respectively. The substitution of titanium with zirconium caused a decrease in the lattice spacing (d_{100}) and lattice parameter (a_0), with a remarkable decrease in the wall thickness values, whereas the pore dimensions are similar (**Table 1**). **Figures 1e-h** report representative TEM images of the aluminosilicate samples (ferrierite and Al-MCM-41), in which an elongated morphology for the ferrierite particles, and a well-defined mesostructure for the Al-MCM-41 sample are visible. TEM images of the TiO_2 and $Ti_{0.77}Zr_{0.23}O_2$ samples showed a well-defined honeycomb structure with similar pore dimensions of about 4 nm (**Figure 2e-h**).

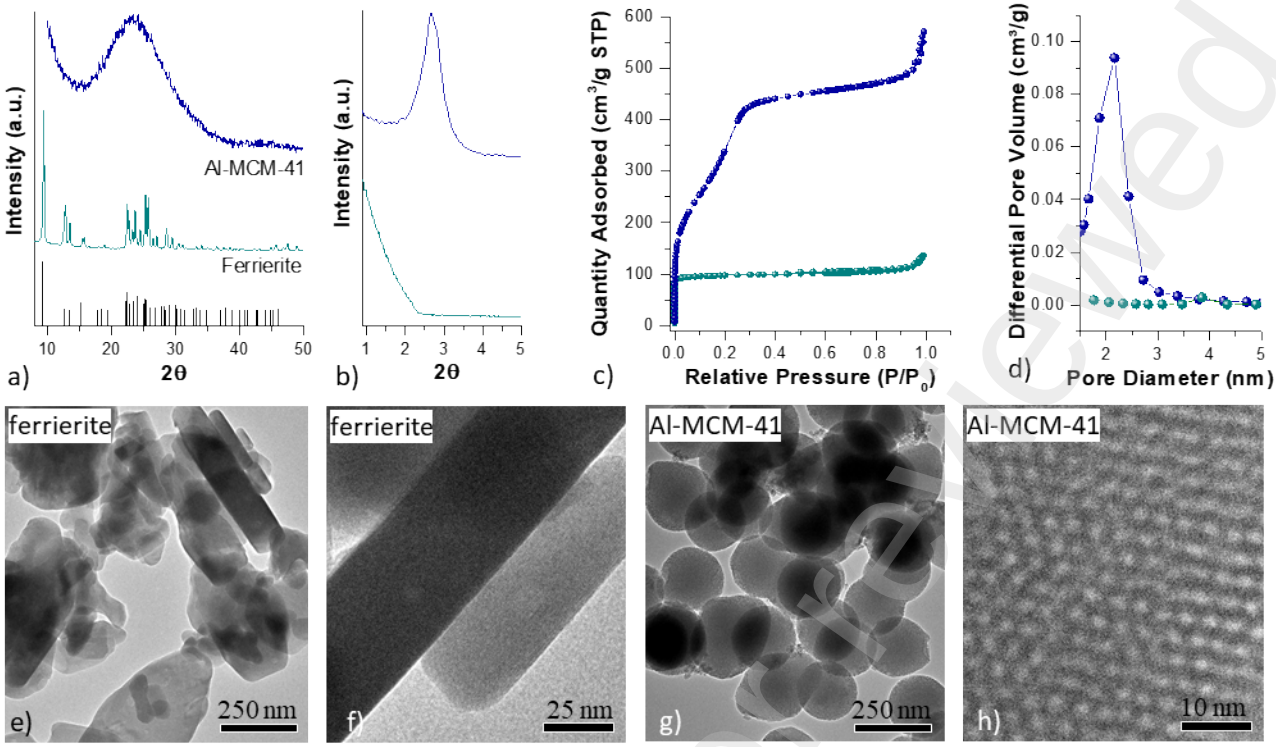

Figure 1. WA-XRD (a) and SA-XRD (b) patterns, nitrogen-physisorption isotherms (c), BJH pore size distributions (d), TEM images of the aluminosilicate samples ferrierite (e,f) and Al-MCM-41 (g,h).

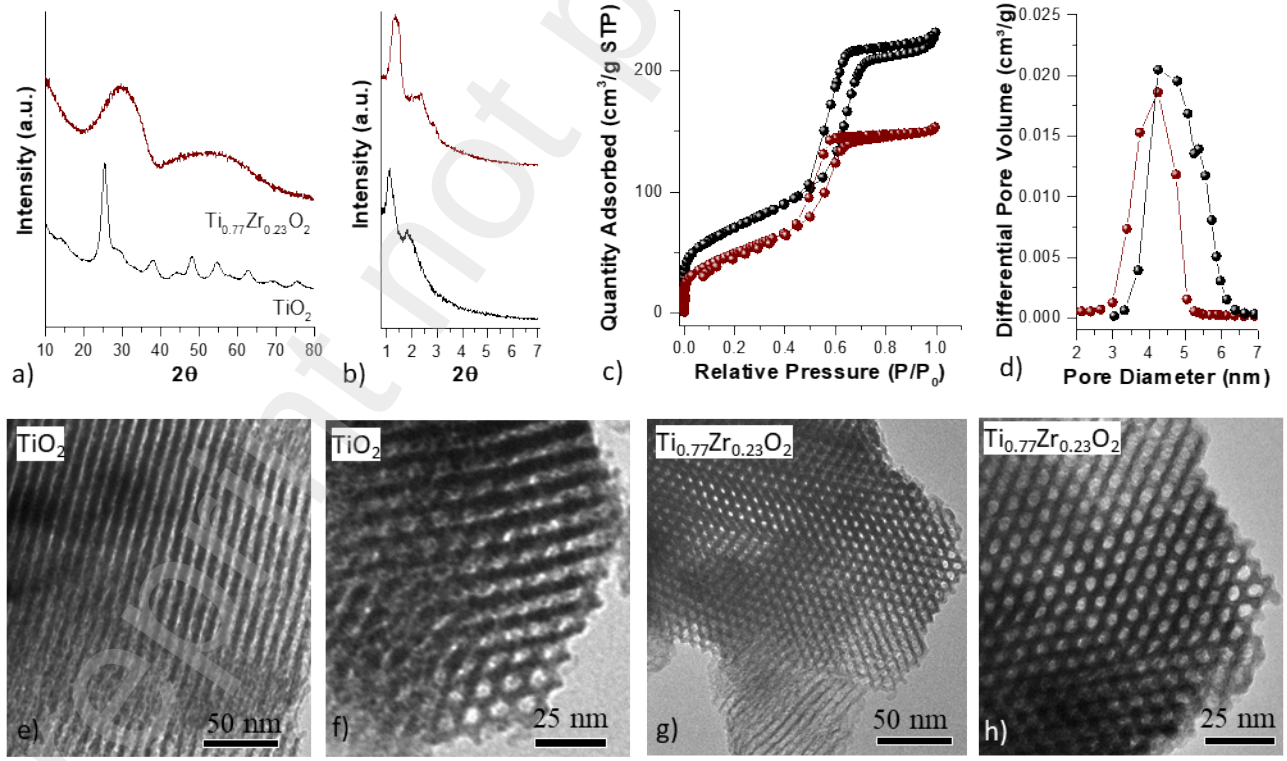

Figure 2. WA-XRD (a) and SA-XRD (b) patterns, nitrogen-physisorption isotherms (c), BJH pore size distributions (d), TEM images of the mesostructured titanium oxide-based samples TiO_2 (e,f) and $Ti_{0.77}Zr_{0.23}O_2$ (g,h).

Table 1. Surface area (SA), pore volume (V_P), pore diameter (D_p), wall thickness (T_w), lattice spacing (d_{100}), and hexagonal unit cell parameter (a_0) for all the samples.

Sample	Typology of isotherm	SA ($m^2\ g^{-1}$)	V_p ($cm^3\ g^{-1}$)	D_p (nm)	T_w (nm)	d_{100} (nm)	a_0 (nm)
Ferrierite	I	415	0.1	0.4	-	-	-
Al-MCM-41	IVB	1246	0.7	2.2	1.1	3.3	3.8
TiO_2	IVA	273	0.3	3.9	4.8	7.5	8.7
$Ti_{0.77}Zr_{0.23}O_2$	IVA	183	0.2	4.2	3.6	6.8	7.8

Relative standard deviation: %RSD(SA)=2.1%; %RSD (V_p)=1.1%; %RSD (D_p)=1.8%. d_{100} and a_0 were obtained from X-ray diffraction data.

3.2 Study of the acidic properties

The acidic properties of the samples were investigated using ammonia-adsorption microcalorimetry and FTIR-monitored pyridine adsorption. **Figure 3a** reports the calorimetric curves obtained by plotting the differential heat of adsorption (Q_{diff}) *vs.* ammonia coverage (n_A, µmol g^{-1}). All the samples showed high initial values of Q_{diff} (> 230 kJ mol^{-1}) that suggest the existence of a small fraction of very strong acidic sites. Except for ferrierite and TiO_2, for which a quasi-plateau was observed between 150 and 110 kJ mol^{-1} and 87 and 77 kJ mol^{-1} respectively (indicative of the presence of isoenergetic acidic sites), the other curves showed a continuous decrease in Q_{diff} as the coverage increases, which points out the heterogeneity of the surface acidic sites from the energetic point of view. In the present case, the cut-off value between specific and non-specific (physisorption) adsorbent/adsorbate interactions is assumed equal to 70 kJ mol^{-1}, which corresponds to the initial value of the heat released during ammonia adsorption experiments on a non-acidic reference sample of pure silica.[13] Therefore, the fraction of ammonia uptake at values of differential heat below 70 kJ mol^{-1} were neglected in the assessment of the acidic sites concentration n_A, and the results are summarized in **Table 2**.

It can be noticed that ferrierite is the most acidic sample, featuring the highest amount of NH_3 adsorbed (1539 µmol g^{-1}). Compared to ferrierite, a moderately lower amount of total acidic sites can be observed for the TiO_2 sample (1168 µmol g^{-1}). Significantly lower amounts of total acidic sites were observed for $Ti_{0.77}Zr_{0.23}O_2$ (504 µmol g^{-1}) and Al-MCM-41 (416 µmol g^{-1}).

Furthermore, the amount of sites on which NH_3 is irreversibly adsorbed ($n_{A,irr}$) was also calculated from the microcalorimetric data (**Table 2**). It is worthy of note that TiO_2 shows the highest concentration of $n_{A,irr}$ (934 µmol g^{-1}), which accounts for 80% of the total acidic sites, quite far from

the value of $Ti_{0.77}Zr_{0.23}O_2$ (49%). A high percentage of $n_{A,irr}$ (69%) was also observed for Al-MCM-41, despite its lower amount of total acidic sites. The lowest percentage of irreversible acidic sites (45%) is shown by ferrierite. However, by expressing the ammonia coverage as µmol m^{-2}, (**Figure 3b**) it results that, due to its much higher surface area, for Al-MCM-41 the surface concentration of acidic sites on which NH_3 is irreversibly adsorbed is one order of magnitude lower than that of the other catalysts in the series, being the values of $n_{A,irr}$ in the order TiO_2 (3.42 µmol m^{-2}) > Ferrierite (1.67 µmol m^{-2}) > $Ti_{0.77}Zr_{0.23}O_2$ (1.36 µmol m^{-2}) >> Al-MCM-41 (0.23 µmol m^{-2}).

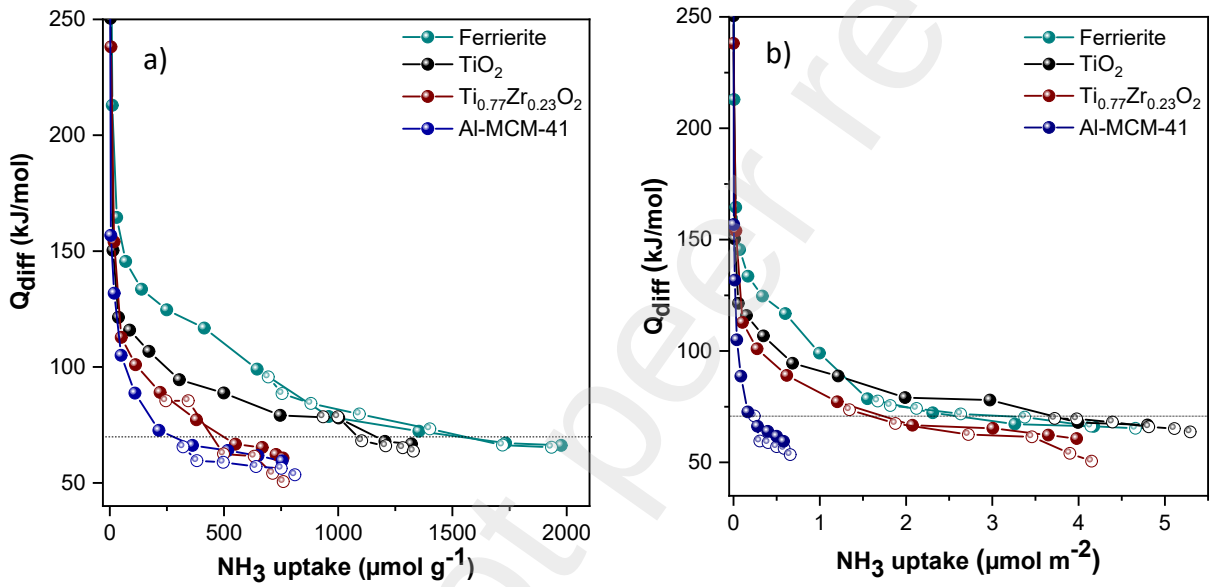

Figure 3. Differential heat (Q_{diff}) vs. uptake for ammonia adsorption expressed in µmol g^{-1} (a) and µmol m^2 (b) for the samples ferrierite, Al-MCM-41, TiO_2 and $Ti_{0.77}Zr_{0.23}O_2$. Open symbols refer to readsorption after overnight evacuation. Dash lines refers to the cut-off value between physisorption and chemisorption (70 kJ mol^{-1}).

Table 2. Ammonia-adsorption microcalorimetric results for the samples ferrierite, Al-MCM-41, TiO_2 and $Ti_{0.77}Zr_{0.23}O_2$.

Sample	$n_{A,tot}$[a] (µmol g^{-1})	$n_{A,tot}$[a] (µmol m^{-2})	$n_{A,irr}$[b] (µmol g^{-1})	$n_{A,irr}$[b] (µmol m^{-2})	$n_{A,irr}$/ $n_{A,tot}$ (%)
Ferrierite	1539	3.71	694	1.67	45
Al-MCM-41	416	0.32	286	0.23	69
TiO_2	1168	4.27	934	3.42	80
$Ti_{0.77}Zr_{0.23}O_2$	504	2.75	248	1.36	49

[a] *Total amount of acidic sites: $Q_{diff} \geq 70$ kJ/mol.*
[b] *Amount of irreversibly adsorbed NH_3.*

The acidic properties of the catalysts were further studied through FTIR-monitored pyridine adsorption; **Figure 4a, 4b** display the spectra recorded on the samples in the 1700-1400 cm^{-1} wavenumber range after saturation and subsequent desorption of pyridine (probe molecule) at room temperature. The spectra are characterized by different FTIR signals ascribable to pyridine in its coordinatively bonded (Lewis), pyridinium ion (PyH^+, Bronsted) or hydrogen-bonded form (physisorption) [43,44].

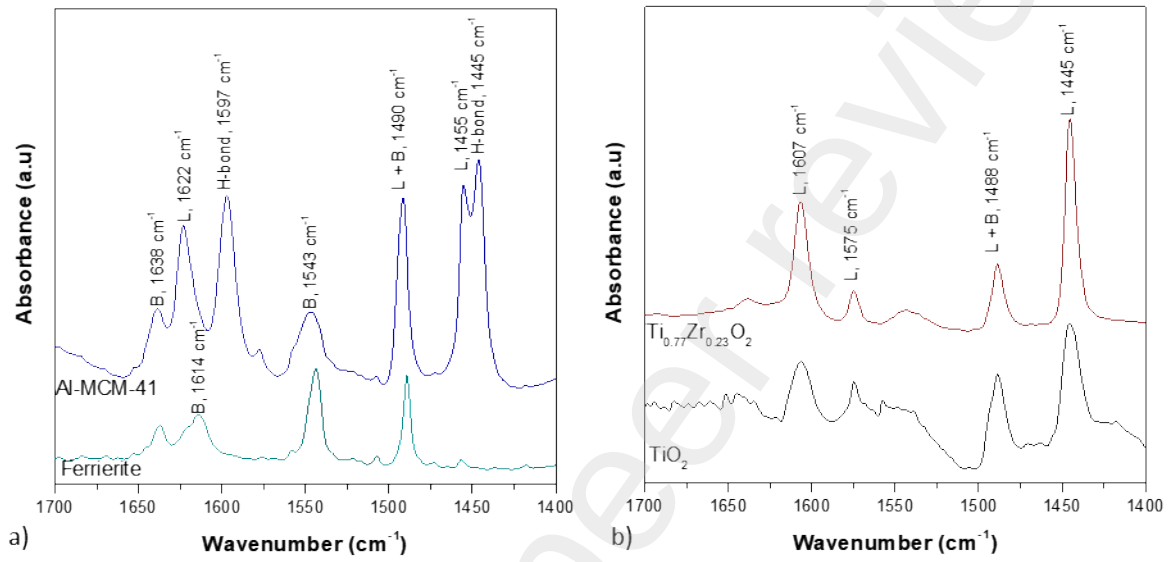

Figure 4. FTIR spectra of the samples ferrierite and Al-MCM-41, (a) TiO_2 and $Ti_{0.77}Zr_{0.23}O_2$ (b) after saturation and subsequent desorption. B, L and H-bond label signals associated with Brønsted acidity, Lewis acidity and hydrogen bonding, respectively.

The spectrum recorded on ferrierite shows clear signals associated to Brønsted acidity (1543 cm^{-1}), and almost neglectable Lewis acidity (1455 cm^{-1}) (**Figure 4a**). The quantification of the two contributions was performed as reported in the literature [45], in which the molar extinction coefficients for Lewis and Brønsted acidic sites are given as 2.22 and 1.67 cm μmol^{-1}, respectively. As expected, Brønsted acidic sites were predominant (96%), with a very low contribution of Lewis acidity (4%). On the contrary, the sample Al-MCM-41 showed the presence of both Brønsted (1543 cm^{-1}) and Lewis acidity (1455 cm^{-1}), as well as a pronounced H-bond signal (1445 cm^{-1}) (**Figure 4a**). To evaluate these contributions, and compare them with the literature [46], the quantification of the acidic sites was carried out as reported in the cited article [46], (excluding H-bond from the quantification and considering the above-mentioned molar extinction coefficients for Lewis and Brønsted acidity). The obtained amounts of Lewis (66%) and Brønsted (34%) acidic sites are comparable with those reported in the literature [46]. Since tetracoordinated aluminum only leads to Brønsted acidity, the Lewis acidity can be attributed to the presence of extra-framework aluminum oxide or aluminum bonded with < 4 SiO_4^{4-} tetrahedra [46]. Therefore, the presence of a

crystalline framework in ferrierite guarantees a high percentage of tetracoordinated aluminum (96% of Brønsted acidic sites); on the other hand, the amorphous nature of Al-MCM-41 leads to the formation of a high amount (66%) of Lewis acidic sites. FTIR spectra of TiO_2 and $Ti_{0.77}Zr_{0.23}O_2$ (**Figure 4b**) clearly highlighted the typical bands centered at about 1445, 1575 and 1607 cm^{-1} ascribable to electron-accepting sites (Lewis acidity). According to the literature [44], the two intense bands at about 1445 and 1607 cm^{-1} are ascribable to strong Lewis sites, while the band at 1575 cm^{-1} is related to weak Lewis sites. However, since the spectra show a broad and weak signal located at about 1540 cm^{-1} it is not possible to exclude the presence of a minor amount of Brønsted acidic sites.

3.3 Catalytic performances of dehydration catalysts

CZA was then tested for the CO_2-to-dimethyl ether (DME) one-pot process in form of a physical mixture with the different acidic dehydration catalysts (ferrierite, Al-MCM-41, mesostructured TiO_2, or mesostructured $Ti_{0.77}Zr_{0.23}O_2$). In comparison with CZA alone, similar CO_2 conversion values were obtained with all the physical mixtures, except for the CZA-TiO_2 sample, which showed a lower value of X_{CO2} (**Figure 5**). An ideal dehydration catalyst should convert all the formed methanol into DME, moving the hydrogenation step toward the production of more methanol and significantly decreasing the production of CO. Indeed, the addition of ferrierite to CZA caused a 10 mol% drop in CO selectivity (**Figure 5**), ascribable to the subtraction of methanol from the reaction environment that, besides favoring the conversion of CO_2 to further methanol, limits its decomposition to CO over the CuO-based redox phase [11]. By converse, the addition of the other dehydration catalysts to CZA did not show any remarkable variation in terms of CO selectivity. Concerning DME formation, the CZA-ferrierite mixture still showed a better performance (S_{DME} = 38 mol%) compared to the physical mixtures derived from the mesostructured samples (Al-MCM-41, TiO_2, and $Ti_{0.77}Zr_{0.23}O_2$), for which selectivity values in the range 7.5 - 10.5 mol% were found. These results were correlated with the amount, strength, and nature of the acidic sites, as well as with the structural and textural properties.

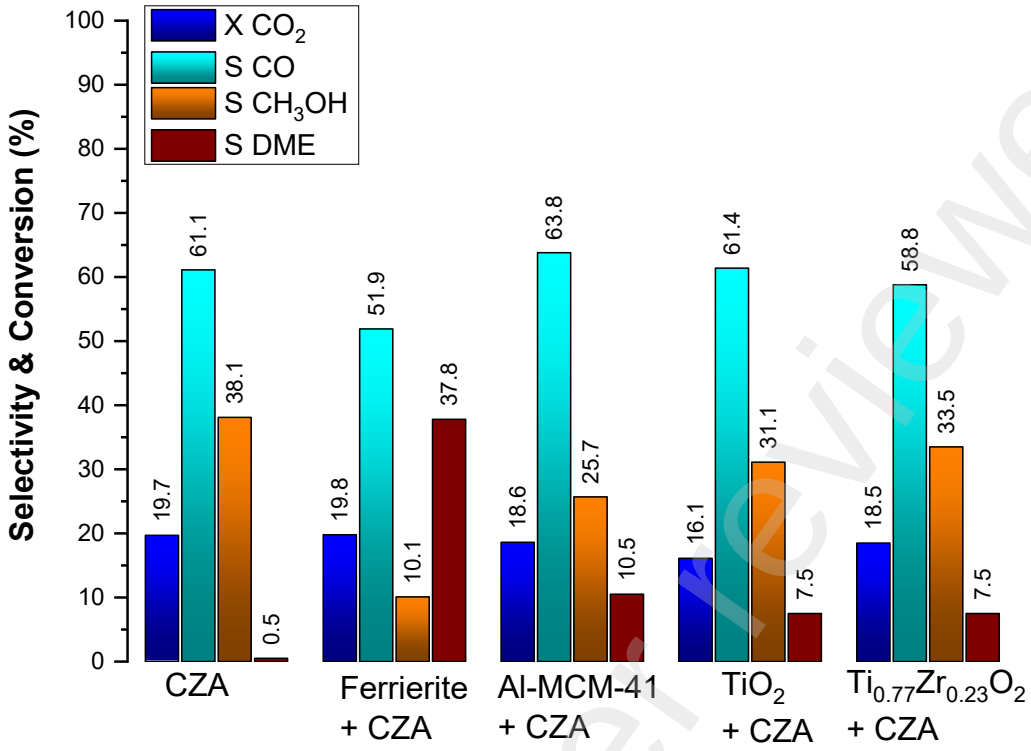

Figure 5. Mean values of CO_2 conversion and selectivity to CO, methanol, and DME after 36 h of test for CZA and physical mixtures (CZA-dehydration catalyst) excluding the first 3h of test. Catalytic conditions: temperature: 250 °C, pressure: 3.0 MPa; GHSV: 12000 $Ncm^3\ g_{cat}^{-1}\ h^{-1}$ in the case of CZA test and 6000 $Ncm^3\ g_{cat}^{-1}\ h^{-1}$ for the physical mixtures tests. Weight Ratio CZA: dehydrant: 1:1.

The higher catalytic performances of the CZA-ferrierite mixture in terms of selectivity to DME (S_{DME}, 37.8 mol%) can be ascribed to its acidic site type (Brønsted, **Figure 4**), their high amount (1539 µmol g^{-1}, **Table 2**), and the presence of an isoenergetic group of sites, according to the results extracted from the combined use of the ammonia-adsorption microcalorimetry and FTIR-monitored adsorption of pyridine. Even though, in the literature, performances of ferrierite resulted to be less affected by the formation of coke than those of other zeolites (MFI and MOR), due to its 2D pore structure [16,47–49], in our conditions a slight gradual decrease of the catalytic performances in terms of DME selectivity from 39.1 mol% (value at 3 h) to 36.5 mol% (value at 36 h) was detected, as shown in **Figure S3**. In order to exclude the contribution of coke, CHN analysis was performed on the spent CZA-ferrierite physical mixture and on its components before the catalytic test. As shown in the supporting information (**Table S3**) the carbon content in the CZA-ferrierite mixture can be entirely attributed to the carbon present in CZA; coke formation was thus excluded, confirming the data reported in the literature by other authors [48]. The decrease in DME selectivity can then be related to a slight worsening of the textural properties of the physical mixture induced by the hydrogenation reaction, generating a decrease of the surface area and the pore volume, as evinced

by the comparison between the nitrogen-physisorption isotherms of the pristine mixture and the isotherms of the spent mixture (CZA, α-Al_2O_3 and ferrierite, **Table S4, Figure S4**).

Among the mesostructured catalysts, Al-MCM-41 showed the best catalytic behavior in terms of DME selectivity. However, despite the significantly superior textural properties, Al-MCM-41 is less selective towards DME (10.5 mol% S_{DME}) than ferrierite (37.8 mol% S_{DME}). This is mainly ascribable to the much higher total number of acidic sites and to the presence of a family of isoenergetic Brønsted sites of moderate strength on the zeolite, deriving from its intrinsic crystalline order. On the other side, the amorphous nature of Al-MCM-41 justifies both the energetic heterogeneity of the acidic sites and the co-existence of Brønsted (66%) and Lewis sites (33%). The gradual worsening of the DME production, observed during the first 7 h of test for Al-MCM-41 (**Figure S5**), could be ascribed to the deactivation of its Lewis acidic sites, to the formation of carbonaceous residues and/or to the gradual collapse of its pore structure (**Figure S6, Table S4**); however, it is important to point out that, during the other 29 h of test, the performances were stable (**Figure S5**). This trend has been observed also by some authors [22,50] and ascribed, in the case of Bedoya *et al.* [50], to the formation of carbonaceous species. The CZA-TiO_2 mixture showed the lowest performances among all catalysts; indeed, despite the promising catalytic performances during the first hours of the test, a remarkable worsening in terms of CO_2 conversion (from 19.7 mol% to 13.8 mol%) and DME selectivity (from 16.3 mol% to 5.1 mol%) was observed during the long-lasting test (36 h) (**Figure S7**). Furthermore, in this case, a significant worsening of the textural properties was observed after the reaction (**Figure S8, Table S4**). On the contrary, $Ti_{0.77}Zr_{0.23}O_2$ presented steady performances (**Figure S9**) and a mean value of DME selectivity similar to that of TiO_2, associated with the lowest CO selectivity (58.8 mol%) among all mesostructured catalysts, even slightly lower than that of pure CZA (61.1 mol%); the textural properties of $Ti_{0.77}Zr_{0.23}O_2$ showed only a minor worsening after the reaction (**Figure S10, Table S4**). These findings can be correlated with the acidic properties of the two samples: though TiO_2 and $Ti_{0.77}Zr_{0.23}O_2$ both possess Lewis acidic sites only, there are remarkable differences in their amount (1168 and 504 µmol g^{-1} of total acidic sites, respectively) and strength (934 and 248 µmol g^{-1} of irreversible acidic sites, respectively) (**Table 2**). Indeed, the higher initial catalytic activity of TiO_2 can be associated with its high amount of total acidic sites; anyway the high percentage of irreversible acidic sites (about 80%), (**Table 2**), suggests a strong interaction with the water produced in both the hydrogenation and dehydration steps, which leads to detrimental effects in the conversion of CO_2 and the production of DME during the catalytic run. On the contrary, the lower initial performances, which however are steady during the

whole test (7.5 mol% S_{DME}), showed by the binary oxide $Ti_{0.77}Zr_{0.23}O_2$ can be ascribed to the lower amount and percentage of irreversible acidic sites (about 50%) that increase its water tolerance under the high-pressure conditions of the catalytic test. This effect can be ascribed to the insertion of zirconium, as already reported by other authors [19] for the dehydration of methanol to DME at atmospheric pressure over non-mesostructured Ti-ZrO_2 samples. The authors highlighted that the water tolerance is enhanced by increasing the amount of zirconium. Following these assumptions, a Ti-Zr mixed oxide with a higher amount of Zr ($Ti_{0.23}Zr_{0.77}O_2$) was tested and, as expected, its catalytic performances (**Figure S11**) proved to be the most stable among all catalysts. $Ti_{0.23}Zr_{0.77}O_2$, like in the case of $Ti_{0.77}Zr_{0.23}O_2$, showed a slight worsening of its textural properties after the reaction (**Figure S12**). The catalytic results obtained for the two mesostructured amorphous catalysts (Al-MCM-41 and $Ti_{0.77}Zr_{0.23}O_2$) indicate that the presence of Brønsted acidic sites in Al-MCM-41 causes higher dehydration performances in terms of DME selectivity, despite the similar amount of total acidic sites and the significantly lower surface concentration for Al-MCM-41. This comparison confirmed that Brønsted acidic sites are more efficient than Lewis sites towards methanol dehydration.

In the light of the above, several points are to be considered in the evaluation of the catalysts, such as (I) stability of the catalyst, (II) CO_2 conversion, (III) CO, CH_3OH, and DME selectivity, with the last two points enclosed in the yield, that can be reasonably expressed as both DME yield and DME + CH_3OH yield, being also methanol a valuable product. **Table S5** reports these values, from which it is possible to evince that, among the mesostructured dehydration catalysts, Al-MCM-41 is the one that shows the higher DME yield (2.0%), while $Ti_{0.77}Zr_{0.23}O_2$ shows the highest DME + CH_3OH yield (7.6%), and steady performances during the test.

4. Conclusions

In this work, several mesostructured acidic oxides with different chemical compositions and textural properties have been synthesized, characterized, and tested as dehydration catalysts in mixture with a commercial redox catalyst (CZA) for the one-pot DME production from CO_2; their catalytic performances have been compared with those of a commercial dehydration zeolite catalyst (ferrierite). In the light of the obtained data, we can conclude that:

1) The comparison between a microporous crystalline material (zeolite ferrierite) and a mesostructured amorphous aluminosilicate (Al-MCM-41) has pointed out that the microporous

crystalline material (ferrierite) demonstrated much better catalytic performances for methanol dehydration due to the high amount of isoenergetic Brønsted acidic sites.

2) The comparison between the mesostructured crystalline TiO_2 and the amorphous Ti-Zr oxide $Ti_{0.77}Zr_{0.23}O_2$ proved that, despite the presence of mostly Lewis acidic sites on both samples, with a higher amount for TiO_2, this catalyst shows a progressive decrease in catalytic performances, probably due to its higher acidic strength, which causes an irreversible water adsorption and a consequent deactivation of the acidic sites. The inclusion of Zr in TiO_2 ($Ti_{0.77}Zr_{0.23}O_2$) led to steady catalytic performances, due to a decrease in strength of the acidic sites, which cause a higher water tolerance, and an increase in porous stability.

3) The different typology (Brønsted *vs* Lewis) but comparable amount of acidic sites (416 µmol g^{-1} *vs* 504 µmol g^{-1}) and the amorphous structural nature of Al-MCM-41 and $Ti_{0.77}Zr_{0.23}O_2$ allowed a direct comparison between the two systems, pointing out a higher activity for Brønsted acidic sites towards methanol dehydration.

The main future perspective of this work is the development of bifunctional catalysts using the mesostructured acidic catalysts as supports to disperse the redox phase in form of confined nanoparticles *via* different impregnation routes already set-up on different materials [51,52]. The synthesis of nanocomposite bifunctional catalysts and the assessment of their catalytic performances, in comparison with those of physical mixtures, will allow to determine the effect of the intimate contact between the two phases. Furthermore, the comparison of mesostructured nanocomposites with zeolite-based composite catalysts, will permit to understand the effect of the nanoparticle confinement inside the mesopores on the performances and the regenerability of composite catalysts.

Other future perspectives include the development of new mesostructured acidic catalysts as Ti-Zr mixed oxides with a high amount of Lewis acidic sites with a moderate strength in order to prevent a strong interaction with water. The promising behavior of Al-MCM-41 can be further enhanced by increasing the number of Brønsted acidic sites and their surface concentration.

Acknowledgements

PON AIM (PON Ricerca e Innovazione 2014–2020 – Azione I.2 – DD n. 407 del 27 febbraio 2018 “Attraction and International Mobility”, Cult-GeoChim project AIM1890410-3), and Sotacarbo S.p.A. are gratefully acknowledged for financing the fellowships of V. Mameli, and C. Cara, respectively. MIUR − National Program PON Ricerca e Innovazione 2014-2020 is acknowledged for the Ph.D. grant

of Fausto Secci (CUP J88D19001040001). The University of Cagliari (UniCA) and Fondazione di Sardegna (FdS) are acknowledged for the financial support – Project: CUP F72F20000240007(2019): "Surface-tailored Materials for Sustainable Environmental Applications". The catalytic tests have been carried out within the "Centre of Excellence on Clean Energy: Phase II" research project (D83C17000370002) led by Sotacarbo and funded by the Regional Government of Sardinia (FSC 2014-2020). We acknowledge the CeSAR (Centro Servizi d'Ateneo per la Ricerca) of the University of Cagliari, Italy, for the TEM and EDX-TEM measurements performed with JEOL JEM 1400 PLUS.

References

[1] I. Miletto, E. Catizzone, G. Bonura, C. Ivaldi, M. Migliori, E. Gianotti, L. Marchese, F. Frusteri, G. Giordano, In situ FT-IR characterization of CuZnZr/ferrierite hybrid catalysts for one-pot CO_2-to-DME conversion, Materials (Basel). 11 (2018). https://doi.org/10.3390/ma11112275.

[2] T.A. Semelsberger, R.L. Borup, H.L. Greene, Dimethyl ether (DME) as an alternative fuel, J. Power Sources. 156 (2006) 497–511. https://doi.org/10.1016/j.jpowsour.2005.05.082.

[3] G.A. Olah, Towards oil independence through renewable methanol chemistry, Angew. Chemie - Int. Ed. 52 (2013) 104–107. https://doi.org/10.1002/anie.201204995.

[4] H. Ham, J. Kim, S.J. Cho, J.H. Choi, D.J. Moon, J.W. Bae, Enhanced Stability of Spatially Confined Copper Nanoparticles in an Ordered Mesoporous Alumina for Dimethyl Ether Synthesis from Syngas, ACS Catal. 6 (2016) 5629–5640. https://doi.org/10.1021/acscatal.6b00882.

[5] A. Álvarez, A. Bansode, A. Urakawa, A. V. Bavykina, T.A. Wezendonk, M. Makkee, J. Gascon, F. Kapteijn, Challenges in the Greener Production of Formates/Formic Acid, Methanol, and DME by Heterogeneously Catalyzed CO_2 Hydrogenation Processes, Chem. Rev. 117 (2017) 9804–9838. https://doi.org/10.1021/acs.chemrev.6b00816.

[6] K. Saravanan, H. Ham, N. Tsubaki, J.W. Bae, Recent progress for direct synthesis of dimethyl ether from syngas on the heterogeneous bifunctional hybrid catalysts, Appl. Catal. B Environ. 217 (2017) 494–522. https://doi.org/10.1016/j.apcatb.2017.05.085.

[7] E. Catizzone, G. Bonura, M. Migliori, F. Frusteri, G. Giordano, CO_2 recycling to dimethyl ether: State-of-the-art and perspectives, Molecules. 23 (2018) 1–28. https://doi.org/10.3390/molecules23010031.

[8] J.M. Spurgeon, B. Kumar, A comparative technoeconomic analysis of pathways for

commercial electrochemical CO_2 reduction to liquid products, Energy Environ. Sci. 11 (2018) 1536–1551. https://doi.org/10.1039/c8ee00097b.

[9] J. Wu, X.D. Zhou, Catalytic conversion of CO_2 to value added fuels: Current status, challenges, and future directions, Cuihua Xuebao/Chinese J. Catal. 37 (2016) 999–1015. https://doi.org/10.1016/S1872-2067(16)62455-5.

[10] J. Sun, G. Yang, Y. Yoneyama, N. Tsubaki, Catalysis Chemistry of Dimethyl Ether Synthesis, ACS Catal. 4 (2014) 3346–3356. https://doi.org/10.1021/cs500967j.

[11] F. Arena, G. Mezzatesta, G. Zafarana, G. Trunfio, F. Frusteri, L. Spadaro, Effects of oxide carriers on surface functionality and process performance of the Cu-ZnO system in the synthesis of methanol via CO_2 hydrogenation, J. Catal. 300 (2013) 141–151. https://doi.org/10.1016/j.jcat.2012.12.019.

[12] E. Catizzone, C. Freda, G. Braccio, F. Frusteri, G. Bonura, Dimethyl ether as circular hydrogen carrier: Catalytic aspects of hydrogenation/dehydrogenation steps, J. Energy Chem. 58 (2021) 55–77. https://doi.org/10.1016/j.jechem.2020.09.040.

[13] U. Mondal, G.D. Yadav, Perspective of dimethyl ether as fuel: Part II- analysis of reactor systems and industrial processes, J. CO_2 Util. 32 (2019) 299–320. https://doi.org/10.1016/j.jcou.2019.02.003.

[14] E. Catizzone, G. Bonura, M. Migliori, F. Frusteri, G. Giordano, CO_2 Recycling to Dimethyl Ether: State-of-the-Art and Perspectives, Molecules. 23 (2017) 31. https://doi.org/10.3390/molecules23010031.

[15] N. Mota, E. Millán Ordoñez, B. Pawelec, J.L.G. Fierro, R.M. Navarro, Direct Synthesis of Dimethyl Ether from CO_2: Recent Advances in Bifunctional/Hybrid Catalytic Systems, Catalysts. 11 (2021) 411. https://doi.org/10.3390/catal11040411.

[16] E. Catizzone, A. Aloise, E. Giglio, G. Ferrarelli, M. Bianco, M. Migliori, G. Giordano, MFI vs. FER zeolite during methanol dehydration to dimethyl ether: The crystal size plays a key role, Catal. Commun. 149 (2021) 106214. https://doi.org/10.1016/j.catcom.2020.106214.

[17] E. Catizzone, M. Migliori, A. Purita, G. Giordano, Ferrierite vs. γ-Al_2O_3: The superiority of zeolites in terms of water-resistance in vapour-phase dehydration of methanol to dimethyl ether, J. Energy Chem. 30 (2019) 162–169. https://doi.org/10.1016/j.jechem.2018.05.004.

[18] Y. Fu, T. Hong, J. Chen, A. Auroux, J. Shen, Surface acidity and the dehydration of methanol to dimethyl ether, Thermochim. Acta. 434 (2005) 22–26.

https://doi.org/10.1016/j.tca.2004.12.023.

[19] V. Vishwanathan, H.S. Roh, J.W. Kim, K.W. Jun, Surface properties and catalytic activity of TiO_2-ZrO_2 mixed oxides in dehydration of methanol to dimethyl ether, Catal. Letters. 96 (2004) 23–28. https://doi.org/10.1023/B:CATL.0000029524.94392.9f.

[20] Y. Xu, P. Yang, H. Zhang, Z. Deng, Atomic Layer Deposition Synthesis of Alumina-Modified SBA-15 and its Catalytic Reactivity Toward Methanol Dehydration, Synth. React. Inorganic, Met. Nano-Metal Chem. 41 (2011) 1033–1038. https://doi.org/10.1080/15533174.2011.591340.

[21] A. Gharibi Kharaji, M. Beheshti, S. Tangestani-nejad, O. Görke, H.R. Godini, Adjusting acidity and porosity of Al-SBA-15 catalyst for methanol to dimethyl ether reaction, Asia-Pacific J. Chem. Eng. 15 (2020) 1–13. https://doi.org/10.1002/apj.2541.

[22] S.P. Naik, V. Bui, T. Ryu, J.D. Miller, W. Zmierczak, Al-MCM-41 as methanol dehydration catalyst, Appl. Catal. A Gen. 381 (2010) 183–190. https://doi.org/10.1016/j.apcata.2010.04.007.

[23] Y. Sang, H. Li, M. Zhu, K. Ma, Q. Jiao, Q. Wu, Catalytic performance of metal ion doped MCM-41 for methanol dehydration to dimethyl ether, J. Porous Mater. 20 (2013) 1509–1518. https://doi.org/10.1007/s10934-013-9737-8.

[24] J. Weglarski, J. Datka, H. He, J. Klinowski, IR spectroscopic studies of the acidic properties of the mesoporous molecular sieve MCM-41, J. Chem. Soc. Faraday Trans. 92 (1996) 5161. https://doi.org/10.1039/ft9969205161.

[25] J. Wang, L. Huang, H. Chen, Q. Li, Acid function of Al-MCM-41 supported platinum catalysts in hydrogenation of benzene, toluene and o-xylene, Catal. Letters. 55 (1998) 157–163. https://doi.org/10.1023/A:1019030811920.

[26] K. Góra-Marek, M. Derewiński, P. Sarv, J. Datka, IR and NMR studies of mesoporous alumina and related aluminosilicates, Catal. Today. 101 (2005) 131–138. https://doi.org/10.1016/j.cattod.2005.01.010.

[27] J.W. Bae, S.H. Kang, Y.J. Lee, K.W. Jun, Synthesis of DME from syngas on the bifunctional Cu-ZnO-Al_2O_3/Zr-modified ferrierite: Effect of Zr content, Appl. Catal. B Environ. 90 (2009) 426–435. https://doi.org/10.1016/j.apcatb.2009.04.002.

[28] J. Sun, G. Yang, Q. Ma, I. Ooki, A. Taguchi, T. Abe, Q. Xie, Y. Yoneyama, N. Tsubaki, Fabrication of active Cu-Zn nanoalloys on H-ZSM5 zeolite for enhanced dimethyl ether synthesis via

syngas, J. Mater. Chem. A. 2 (2014) 8637–8643. https://doi.org/10.1039/c3ta14936f.

[29] M. Cai, A. Palčić, V. Subramanian, S. Moldovan, O. Ersen, V. Valtchev, V. V. Ordomsky, A.Y. Khodakov, Direct dimethyl ether synthesis from syngas on copper-zeolite hybrid catalysts with a wide range of zeolite particle sizes Dedicated to Professor Jean-Pierre Gilson on the occasion of his 60th birthday., J. Catal. 338 (2016) 227–238. https://doi.org/10.1016/j.jcat.2016.02.025.

[30] G. Bonura, M. Migliori, L. Frusteri, C. Cannilla, E. Catizzone, G. Giordano, F. Frusteri, Acidity control of zeolite functionality on activity and stability of hybrid catalysts during DME production via CO_2 hydrogenation, J. CO_2 Util. 24 (2018) 398–406. https://doi.org/10.1016/j.jcou.2018.01.028.

[31] I. Barroso-Martín, A. Infantes-Molina, F. Jafarian Fini, D. Ballesteros-Plata, E. Rodríguez-Castellón, E. Moretti, Silica-Related Catalysts for CO_2 Transformation into Methanol and Dimethyl Ether, Catalysts. 10 (2020) 1282. https://doi.org/10.3390/catal10111282.

[32] A.M. Hengne, K.D. Bhatte, S. Ould-Chikh, Y. Saih, J.M. Basset, K. Huang, Selective Production of Oxygenates from Carbon Dioxide Hydrogenation over a Mesoporous-Silica-Supported Copper-Gallium Nanocomposite Catalyst, ChemCatChem. 10 (2018) 1360–1369. https://doi.org/10.1002/cctc.201701679.

[33] H. Jiang, H. Bongard, W. Schmidt, F. Schüth, One-pot synthesis of mesoporous Cu–γ-Al_2O_3 as bifunctional catalyst for direct dimethyl ether synthesis, MICROPOROUS MESOPOROUS Mater. 164 (2012) 3–8. https://doi.org/10.1016/j.micromeso.2012.08.004.

[34] H. Ham, J. Kim, S.J. Cho, J.-H. Choi, D.J. Moon, J.W. Bae, Enhanced Stability of Spatially Confined Copper Nanoparticles in an Ordered Mesoporous Alumina for Dimethyl Ether Synthesis from Syngas, ACS Catal. 6 (2016) 5629–5640. https://doi.org/10.1021/acscatal.6b00882.

[35] E. Rombi, M.G. Cutrufello, C. Cannas, M. Casu, D. Gazzoli, M. Occhiuzzi, R. Monaci, I. Ferino, Modifications induced by pretreatments on Au/SBA-15 and their influence on the catalytic activity for low temperature CO oxidation., Phys. Chem. Chem. Phys. 11 (2009) 593–602. https://doi.org/10.1039/b813982b.

[36] M.A. Vacca, C. Cara, V. Mameli, M. Sanna Angotzi, M.A. Scorciapino, M.G. Cutrufello, A. Musinu, V. Tyrpekl, L. Pala, C. Cannas, Hexafluorosilicic Acid (FSA): From Hazardous Waste to Precious Resource in Obtaining High Value-Added Mesostructured Silica, ACS Sustain. Chem. Eng. 8 (2020) 14286–14300. https://doi.org/10.1021/acssuschemeng.0c03218.

[37] C. Cara, E. Rombi, A. Musinu, V. Mameli, A. Ardu, M. Sanna Angotzi, L. Atzori, D. Niznansky, H.L. Xin, C. Cannas, MCM-41 support for ultrasmall γ-Fe_2O_3 nanoparticles for H_2S removal, J. Mater. Chem. A. 5 (2017) 21688–21698. https://doi.org/10.1039/C7TA03652C.

[38] C. Cara, E. Rombi, A. Ardu, M.A. Vacca, C. Cannas, Sub-Micrometric MCM-41 Particles as Support to Design Efficient and Regenerable Maghemite-Based Sorbent for H_2S Removal, J. Nanosci. Nanotechnol. 19 (2019) 5035–5042. https://doi.org/10.1166/jnn.2019.16800.

[39] C. Cara, V. Mameli, E. Rombi, N. Pinna, M. Sanna Angotzi, D. Nižňanský, A. Musinu, C. Cannas, Anchoring ultrasmall FeIII-based nanoparticles on silica and titania mesostructures for syngas H_2S purification, Microporous Mesoporous Mater. 298 (2020) 110062. https://doi.org/10.1016/j.micromeso.2020.110062.

[40] M. Mureddu, F. Ferrara, A. Pettinau, Highly efficient CuO/ZnO/ZrO_2@SBA-15 nanocatalysts for methanol synthesis from the catalytic hydrogenation of CO_2, Appl. Catal. B Environ. 258 (2019) 117941. https://doi.org/10.1016/j.apcatb.2019.117941.

[41] M. Mureddu, S. Lai, L. Atzori, E. Rombi, F. Ferrara, A. Pettinau, M.G. Cutrufello, Ex-LDH-Based Catalysts for CO_2 Conversion to Methanol and Dimethyl Ether, Catalysts. 11 (2021) 615. https://doi.org/10.3390/catal11050615.

[42] R. Zhang, B. Tu, D. Zhao, Synthesis of Highly Stable and Crystalline Mesoporous Anatase by Using a Simple Surfactant Sulfuric Acid Carbonization Method, Chem. - A Eur. J. 16 (2010) 9977–9981. https://doi.org/10.1002/chem.201001241.

[43] E.P. Parry, An infrared study of pyridine adsorbed on acidic solids. Characterization of surface acidity, J. Catal. 2 (1963) 371–379. https://doi.org/10.1016/0021-9517(63)90102-7.

[44] V. Vishwanathan, H.-S. Roh, J.-W. Kim, K.-W. Jun, Surface Properties and Catalytic Activity of TiO_2 –ZrO_2 Mixed Oxides in Dehydration of Methanol to Dimethyl Ether, Catal. Letters. 96 (2004) 23–28. https://doi.org/10.1023/B:CATL.0000029524.94392.9f.

[45] C.A. EMEIS, Determination of Integrated Molar Extinction Coefficients for IR Absorption Bands of Pyridine Adsorbed on Solid Acid Catalysts, J. Catal 141 (1993) 347-354. https://doi.org/10.1006/jcat.1993.1145.

[46] J.M.R. Gallo, C. Bisio, G. Gatti, L. Marchese, H.O. Pastore, Physicochemical Characterization and Surface Acid Properties of Mesoporous [Al]-SBA-15 Obtained by Direct Synthesis, Langmuir. 26 (2010) 5791–5800. https://doi.org/10.1021/la903661q.

[47] E. Catizzone, A. Aloise, M. Migliori, G. Giordano, Dimethyl ether synthesis via methanol

dehydration: Effect of zeolite structure, Appl. Catal. A Gen. 502 (2015) 215–220. https://doi.org/10.1016/j.apcata.2015.06.017.

[48] M. Migliori, E. Catizzone, A. Aloise, G. Bonura, L. Gómez-Hortigüela, L. Frusteri, C. Cannilla, F. Frusteri, G. Giordano, New insights about coke deposition in methanol-to-DME reaction over MOR-, MFI- and FER-type zeolites, J. Ind. Eng. Chem. 68 (2018) 196–208. https://doi.org/10.1016/j.jiec.2018.07.046.

[49] E. Catizzone, A. Aloise, M. Migliori, G. Giordano, From 1-D to 3-D zeolite structures: performance assessment in catalysis of vapour-phase methanol dehydration to DME, MICROPOROUS MESOPOROUS Mater. 243 (2017) 102–111. https://doi.org/10.1016/j.micromeso.2017.02.022.

[50] J.C. Bedoya, R. Valdez, L. Cota, M.A. Alvarez-Amparán, A. Olivas, Performance of Al-MCM-41 nanospheres as catalysts for dimethyl ether production, Catal. Today. (2021) 1–8. https://doi.org/10.1016/j.cattod.2021.01.010.

[51] M.A. Vacca, C. Cara, V. Mameli, M. Sanna Angotzi, M.A. Scorciapino, M.G. Cutrufello, A. Musinu, V. Tyrpekl, L. Pala, C. Cannas, Hexafluorosilicic Acid (FSA): from Hazardous Waste to Precious Resource in Obtaining High Value-Added Mesostructured Silica, ACS Sustain. Chem. Eng. 8 (2020) 14286–14300. https://doi.org/10.1021/acssuschemeng.0c03218.

[52] M. Mureddu, I. Ferino, A. Musinu, A. Ardu, E. Rombi, M.G. Cutrufello, P. Deiana, M. Fantauzzi, C. Cannas, MeOx /SBA-15 (Me = Zn, Fe): highly efficient nanosorbents for mid-temperature H 2 S removal, J. Mater. Chem. A. 2 (2014) 19396–19406. https://doi.org/10.1039/C4TA03540B.